

## HH 212: SMA OBSERVATIONS OF A REMARKABLE PROTOSTELLAR JET

CHIN-FEI LEE<sup>1</sup>, PAUL T.P. HO<sup>2,3</sup>, HENRIK BEUTHER<sup>4</sup>, TYLER L. BOURKE<sup>3</sup>, NAOMI HIRANO<sup>2</sup>,  
HSIEN SHANG<sup>2</sup>, AND QIZHOU ZHANG<sup>3</sup>

*Draft version October 1, 2018*

## ABSTRACT

HH 212 is a nearby (460 pc) protostellar jet discovered in H<sub>2</sub> powered by a Class 0 source, IRAS 05413-0104, in the L1630 cloud of Orion. It is highly collimated and symmetric with matched pairs of bow shocks on either side of the source. We have mapped it in 850  $\mu$ m continuum, SiO ( $J = 8 - 7$ ), CO ( $J = 3 - 2$ ), SO ( $N_J = 8_9 - 7_8$ ), HCO<sup>+</sup> ( $J = 4 - 3$ ), and H<sup>13</sup>CO<sup>+</sup> ( $J = 4 - 3$ ) emission simultaneously at  $\sim 1''$  resolution with the Submillimeter Array (SMA). Thermal dust emission is seen in continuum around the source, mainly arising from an inner envelope (i.e., the inner part of a previously seen flattened envelope) and a possible disk. The inner envelope is also seen with rotation in CO, HCO<sup>+</sup>, and probably SO. Like H<sub>2</sub> emission, CO and SiO emission are seen along the jet axis but extending closer to the source, tracing the bow shocks with a broad range of velocities and the continuous structures in between. SO emission is seen only around the source, forming a jetlike structure extending along the jet axis from the source, likely tracing the jet near the launching region. The jet is episodic and bending. It may also be slightly precessing as the jetlike SO structure shows a slight S-shaped symmetry about the source. A hint of jet rotation is also seen across the jet axis. Internal outflow shells are seen in CO and HCO<sup>+</sup>, associated with the bow shocks in the inner part of the jet. The bases of the HCO<sup>+</sup> shells are seen with a hint of rotation similar to that seen in the inner envelope, probably consisted mainly of the material extended from the inner envelope and even the possible disk. The bases of the outflow shells are also seen in H<sup>13</sup>CO<sup>+</sup> and even the continuum, probably tracing the dense material extended from around the same regions. Outflow shells are also seen in CO surrounding the jet extending out from the H<sub>2</sub> nebulae seen around the source.

*Subject headings:* stars: formation — ISM: individual: HH 212 — ISM: jets and outflows.

## 1. INTRODUCTION

Protostellar jets are seen associated with low-mass protostars in the early stages of star formation. In spite of numerous studies, their physical properties (e.g., speed, episodic nature, collimation, and angular momentum) are still not well understood (Hartigan et al. 2000). They are believed to be launched from accretion disks around the protostars (Shu et al. 2000; Konigl & Pudritz 2000), allowing us to probe the accretion process, which remains heretofore unresolved, as it requires us to observe directly in the inner parts at the AU scale. The Submillimeter Array (SMA)<sup>5</sup> (Ho et al. 2004), with the capability to probe warm and dense molecular gas at high angular resolution, can be and has been used to study the physical properties of the jets in great detail (Hirano et al. 2006; Palau et al. 2006).

The HH 212 jet, which is nearby (460 pc) in the L1630 cloud of Orion and remarkably well-defined, is one of the best candidates to investigate the physical properties of the jets. It was discovered in shock excited H<sub>2</sub> emission (Zinnecker, McCaughrean, & Rayner 1998), powered by a low-luminosity ( $\sim 14 L_\odot$ ) Class 0 source (or protostar), IRAS 05413-0104. It is highly collimated and highly symmetric with matched pairs of bow shocks on either side of the source. Water masers are seen at the bases of the

jet with proper motions along the jet axis (Claussen et al. 1998). The jet interacts with the ambient material, driving a collimated CO outflow around it (Lee et al. 2000; Lee et al. 2006, hereafter Paper I). Deep observations in H<sub>2</sub> using the Infrared Spectrometer And Array Camera (ISAAC) of the ESO Very Large Telescope (VLT) show a pair of diffuse nebulae near the bases of the jet, probably tracing the outflow cavity walls illuminated by the bright bow shocks around the source (McCaughrean et al. 2002, hereafter MZAML02). The inner part of the jet is also seen in shock excited SiO emission (Chapman et al. 2002; Gibb et al. 2004; Takami et al. 2006) and high-velocity CO emission (Paper I). Since the jet is compact, dense, and warm, high-resolution observations in high- $J$  transition lines of SiO, CO, and other shock tracers are presented here to study its physical properties.

## 2. OBSERVATIONS

Observations toward the HH 212 jet were carried out with the SMA on December 2, 2005 in the compact configuration and on January 14, 2006 in the extended configuration. SiO ( $J = 8 - 7$ ), CO ( $J = 3 - 2$ ), SO ( $N_J = 8_9 - 7_8$ ), HCO<sup>+</sup> ( $J = 4 - 3$ ), and H<sup>13</sup>CO<sup>+</sup> ( $J = 4 - 3$ ) lines were observed simultaneously with 850  $\mu$ m continuum using the 345 GHz band receivers. The rest frequency, upper energy

<sup>1</sup> Harvard-Smithsonian Center for Astrophysics, Submillimeter Array, 645 North A'ohoku, Hilo, HI 96720; cflee@cfa.harvard.edu

<sup>2</sup> Academia Sinica Institute of Astronomy and Astrophysics, P.O. Box 23-141, Taipei 106, Taiwan

<sup>3</sup> Harvard-Smithsonian Center for Astrophysics, 60 Garden Street, Cambridge, MA 02138

<sup>4</sup> Max-Planck-Institute for Astronomy, Königstuhl 17, 69117 Heidelberg, Germany

<sup>5</sup> The Submillimeter Array is a joint project between the Smithsonian Astrophysical Observatory and the Academia Sinica Institute of Astronomy and Astrophysics, and is funded by the Smithsonian Institution and the Academia Sinica.

level, and critical density of these lines are given in Table 1. The receivers have two sidebands, lower and upper, covering the frequency range from 345.5 to 347.5 and from 355.5 to 357.5 GHz, respectively. Combining the two sidebands results in a total bandwidth of 4 GHz centered at 351.5 GHz (or  $\lambda \sim 850 \mu\text{m}$ ). Seven antennas were used in the array, giving baselines with projected lengths ranging from 8.5 to 180 m. Since the primary beam has a size of  $\sim 35''$ , two pointings with a separation of  $18''$  were used to map the inner part of the jet within  $25''$  from the source. For the correlator, 256 spectral channels were used for each 104 MHz chunk, resulting in a velocity resolution of  $\sim 0.35 \text{ km s}^{-1}$  per channel.

The visibility data were calibrated with the MIR package, with Saturn, Uranus, and Quasar 3C454.3 as passband calibrators, Quasar J0530+135 as a gain calibrator, and Uranus as a flux calibrator. The calibrated visibility data were imaged with the MIRIAD package. The dirty maps that were produced from the calibrated visibility data were CLEANed using the Steer clean method, producing the CLEAN component maps. The final maps were obtained by restoring the CLEAN component maps with a synthesized (Gaussian) beam fitted to the main lobe of the dirty beam. With natural weighting, the synthesized beam has a size of  $1''.16 \times 0''.84$  at a position angle (P.A.) of  $38^\circ$ . In some cases, however, in order to study the compact structures (i.e., the jet and the possible disk) in the system, the visibilities with  $uv$  radius shorter than 40 m (or  $\gtrsim 2''.5$ ) are excluded, resulting in a smaller synthesized beam with a size of  $0''.96 \times 0''.69$  at P.A. =  $38^\circ$ . The rms noise level is  $\sim 0.16 \text{ Jy beam}^{-1}$  in the channel maps and  $5 \text{ mJy beam}^{-1}$  in the continuum map. The velocities of the channel maps are LSR. The absolute positional accuracy in our maps is expected to be one tenth of the synthesized beam, or  $\sim 0''.1$ .

### 3. RESULTS

In the following, our results are presented with the  $\text{H}_2$  image made with the VLT (MZAML02) for comparison. The  $\text{H}_2$  image, which shows a clear jet consisting of a chain of bow shocks and sinuous continuous structures in between in great detail, is used as a reference for the jet. Since our observations were carried out about 4 years later than the  $\text{H}_2$  image, the bow shocks, which were found to be moving at  $100\text{--}200 \text{ km s}^{-1}$  or  $0''.045\text{--}0''.09$  per year (MZAML02), might have moved down along the jet axis by  $0''.18\text{--}0''.36$  from their positions in that image. This movement of the bow shocks, however, does not affect significantly our comparison and conclusions, considering that the angular resolution of our observations is  $\sim 1''$  along the jet axis. The  $\text{H}_2$  jet is almost in the plane of the sky, with the blueshifted side to the north and the redshifted side to the south of the source (Zinnecker, McCaughrean, & Rayner 1998). The systemic velocity in this region is assumed to be  $1.7 \pm 0.1 \text{ km s}^{-1}$ , as in Paper I. Throughout this paper, the velocity is relative to this systemic value.

#### 3.1. $850 \mu\text{m}$ Continuum Emission

A continuum source is detected at  $850 \mu\text{m}$  in between the diffuse  $\text{H}_2$  nebulae with an emission peak at  $\alpha_{(2000)} = 05^\text{h}43^\text{m}51^\text{s}404 \pm 0''.1$ ,  $\delta_{(2000)} = -01^\circ02'53''.10 \pm 0''.1$ , and

a total integrated flux of  $0.38 \pm 0.10 \text{ Jy}$  (Fig. 1a). This peak position is within  $0''.1$  from that found at  $\lambda = 3.5 \text{ cm}$  with the VLA at an angular resolution of  $0''.3$  (Galván-Madrid et al. 2004), and is thus considered as the source position throughout this paper. The structure of the continuum source is not well resolved in the restored map. It is better seen in the CLEAN component map, which shows a faint flattened structure with a radius of  $\sim 1''$  (460 AU) perpendicular to the jet axis and a bright unresolved compact structure with a radius  $< 0''.3$  (138 AU) at the center. Faint emission is also seen extending to the northeast and southwest. The faint flattened structure, which is not resolved in the minor axis, may trace the inner envelope, i.e., the inner part of the edge-on flattened envelope seen in Paper I, while the compact structure may trace the envelope further in and a possible disk. The faint emission extending to the northeast and southwest, on the other hand, may trace the material extended from the inner envelope, as discussed later in §4.2. A compact source with an envelope is also seen in the amplitude versus  $uv$  distance plot. However, observations at higher angular resolution are really needed to confirm the structure seen in the CLEAN component map. The spectral energy distribution (SED) of the continuum source (see Fig. 1b and also Paper I) indicates that the continuum emission at  $850 \mu\text{m}$  is mainly thermal dust emission. Assuming a constant temperature, a mass opacity  $\kappa_\nu = 0.1(\nu/10^{12} \text{ Hz})^\beta \text{ cm}^2 \text{ g}^{-1}$  (Beckwith et al. 1990), and a source size of  $1 \text{ arcsec}^2$  for the dust, the SED can be fitted with  $\beta = 1$  and a temperature of  $\sim 48 \text{ K}$ . Thus, the (gas + dust) mass is estimated to be  $\sim 0.08 M_\odot$ , as in Paper I. With  $\beta = 1$ , the bright compact structure at the center may indeed harbor a disk around the source (Jørgensen et al. 2006).

#### 3.2. Jet Axis and Bending

The northern component and southern component of the  $\text{H}_2$  jet are not exactly antiparallel (Figs. 2a and 2b). Their inner parts are misaligned by  $\sim 2^\circ$ , with their axes found to have a P.A. of  $21.5^\circ \pm 0.5^\circ$  and  $203.5^\circ \pm 0.5^\circ$ , respectively, by connecting the source to the inner  $\text{H}_2$  bow shocks out to bow shocks NK7 and SK7. Since their original paths of motion are likely to be antiparallel, this misalignment suggests a presence of a jet bending (see §4.1.6 for possible mechanisms). Assuming both bent by the same degree, their inner parts are both bent by  $\sim 1^\circ$  to the west with the original axis having a P.A. of  $22.5^\circ \pm 1^\circ$ . Note that the bending actually continues further out and beyond bow shocks NB1/2 and SB1/2.

The outer parts of the jet may have different original axis and bending because the tips of bow shocks NB3 and SB4 are on the opposite sides of the axes of the inner parts. The original axis, which can be estimated by connecting the tips of bow shocks NB3 and SB4, is found to have a P.A. greater than that of the inner parts, suggesting that the jet axis might have rotated clockwise more than a few thousands years ago. However, without knowing the source position at the time when bow shocks NB3 and SB4 were formed, we are not able to determine the bending.

#### 3.3. $\text{SiO}$ , $\text{CO}$ , and $\text{SO}$ emission

##### 3.3.1. Morphologies

SiO emission is detected mainly along the jet axis (Fig. 2c). About 70% of the single-dish flux is recovered from our observations, comparing to the Atacama Submillimeter Telescope Experiment (ASTE) observations (Takami et al. 2006). It is detected toward the bow shocks and the continuous structures seen in H<sub>2</sub>. Bow shocks NK2, NK4, SK2, and SK4, which are bright in H<sub>2</sub>, are also bright in SiO. However, bow shocks NK1 and SK1, which are bright and prominent in H<sub>2</sub>, are faint in SiO and only detected on their eastern sides. SiO emission is also detected at  $\sim 1''$  north and south of the source, forming knotty structures labeled knots SN and SS, respectively (see Fig. 3a for the closeup). The knots are spatially unresolved with a diameter (transverse size) of less than  $1''$  (460 AU). A faint elongated structure is seen extending to the southwest from knot SS, fitting in between the wings of bow shock SK1, possibly tracing the “intrinsic” jet itself, but not the shock.

CO emission is detected not only along the jet axis but also toward outflow shells (Fig. 4a). In the following, two velocity ranges, high and low, are selected to show these two components separately. At high velocity (from  $-18.4$  to  $-7.1 \text{ km s}^{-1}$  and from  $3.4$  to  $13.3 \text{ km s}^{-1}$ ), CO emission is seen mainly along the jet axis toward the bow shocks and the continuous structures seen in H<sub>2</sub>, with some coincident with the SiO emission (compare Figs. 2c and 2d). CO emission is also detected at  $\sim 1''$  away from the source (see Fig. 3b for the closeup), associated with knots SN and SS seen in SiO. At low velocity (from  $-4.0$  to  $3.1 \text{ km s}^{-1}$ ), limb-brightened outflow shells (labeled A and B) are seen extending to the north and south, respectively, from the H<sub>2</sub> nebulae (Fig. 4b). They seem to connect to the H<sub>2</sub> bow shocks SB1/2, NK7, and NB1/2 and some further down the jet axis, and are thus probably internal outflow shells driven by them. Throughout this paper, outflow shells are called internal if not driven by the leading bow shocks at the heads of the jet. Near the source, a limb-brightened internal outflow shell is seen in the south connecting to bow shock SK1 (Fig. 4c). Internal outflow shells are also seen in the north but associated with more than one bow shock. The emission extending along the jet axis to bow shock NK1 is unresolved but may trace an internal outflow shell as a counterpart of that extending to bow shock SK1.

SO emission, on the other hand, is detected mainly around the source (Fig. 3c). Jetlike emission is seen along the jet axis extending from the source to the north and south to knots SN and SS, respectively, likely tracing the jet near the launching region. The northern component is shifted slightly to the east and the southern component is shifted slightly to the west of the jet axis, showing a slight S-shaped symmetry about the source.

### 3.3.2. Kinematics

The kinematics of the bow shocks and the continuous structures can be studied with the position-velocity (PV) diagrams of the SiO and CO emission cut along the jet axis (Fig. 5). In the PV diagrams, the CO emission around the systemic velocity, which merges with that of the ambient cloud, and the CO emission from  $7$  to  $9 \text{ km s}^{-1}$ , which merges with that of the foreground ambient cloud with the same velocity range, are resolved out from our observations (see also Paper I). The internal outflow shells (labeled S)

near the source are seen in CO with the velocity magnitude increasing with the distance from the source toward bow shocks NK1, NK2, and SK1 on both the redshifted and blueshifted sides, indicating that the shells around the bow shocks are expanding mainly transversely perpendicular to the jet axis. This is expected for outflow shells driven by jet-driven bow shocks (see, e.g., Lee et al. 2001). The bases of the shells, on the other hand, may also have velocity component parallel to the jet axis.

Like the H<sub>2</sub> emission, the SiO and CO emission toward the bow shocks and the continuous structures are mainly blueshifted in the north and redshifted in the south. They are, however, more blueshifted in the north than redshifted in the south, with a mean (representative) velocity of  $\sim -11 \text{ km s}^{-1}$  in the north while  $7 \text{ km s}^{-1}$  in the south, similar to that seen in the H<sub>2</sub> emission (Takami et al. 2006). The reason for this asymmetry in the velocity is unclear. The SiO emission is seen with a range of velocities toward the bow shocks: bow shocks NK2, NK4, SK2, and SK4 are bright and seen with a velocity range of  $\sim 15 \text{ km s}^{-1}$ , while other bow shocks are faint and seen with a narrower velocity range. The SiO emission is not well resolved, probably some from the bow tips with a broad range of velocities and some from the bow wings with the velocity magnitude decreasing rapidly away from the bow tips. The CO emission is also seen with a range of velocities toward the bow shocks, some with similar and some with narrower velocity range than that of the SiO emission. Some CO emission is probably from the bow tips and some from the bow wings, with some (e.g., bow shocks NK2 and SK2) coincident with the SiO emission. Note that a broad range of velocities is also seen ahead of bow shock NK4 in CO, suggesting that a shock is formed there.

The continuous structures between the bow shocks may trace the “intrinsic” jet itself and thus can be used to study the jet kinematics. In the south, the continuous structure is seen between bow shocks SK1 and SK2 in CO and SiO. The SiO and CO emission there together may show that its velocity increases with the distance from bow shocks SK1 to SK2. In the north, the continuous structures are seen between bow shocks NK1 and NK2 and between bow shocks NK2 and NK4 in CO. Their velocity also seems to increase with the distance from one bow shock to the next.

The kinematics of knots SS and SN around the source can be studied with the PV diagrams of the SiO, CO, and SO emission (Fig. 6). In SiO, knots SN and SS are also seen with a broad range of velocities, but with a lower mean velocity than that seen toward the bow shocks further away. The kinematics of the CO emission is unclear, probably with a velocity magnitude increasing with the distance from the source toward the knots on both blueshifted and redshifted sides. The kinematics of the SO emission is also unclear, probably partly similar to that of the SiO emission and partly similar to that of the CO emission. Observations at higher resolution are really needed to resolve their structures and study the detailed relationship among them.

## 3.4. HCO<sup>+</sup> and H<sup>13</sup>CO<sup>+</sup> emission

### 3.4.1. Morphologies

HCO<sup>+</sup> emission is seen extending to the north from the source surrounding the CO emission that extends to bow

shock NK1 (Fig. 7a). The emission is likely from a limb-brightened shell as seen in the blueshifted emission, but with the east side brighter than the west side (Fig. 7b). It extends to the faint bow shock NF and then to the wings of bow shock NK1. Its base is also seen in continuum coincident with its northeast extension (Fig. 7c). In the south, a similar shell is expected to be seen in  $\text{HCO}^+$ , but it is faint and only seen at the base surrounding the CO shell that extends to bow shock SK1. As in CO, the shell is brighter on the west side. Note that the emission (labeled NW in Fig. 7c) extending to the northwest from the source is almost perpendicular to the jet axis coincident with the continuum emission and thus may arise from the inner envelope.

A shell is also seen in  $\text{H}^{13}\text{CO}^+$  extending to the north from the source, surrounding the east side of the north base of the  $\text{HCO}^+$  shell (Fig. 7d). The emission seen across the source may arise from both the inner envelope and the shell, with the emission peak northwest of the source.

### 3.4.2. Kinematics

As mentioned, the  $\text{HCO}^+$  emission around the source perpendicular to the jet axis may arise from the inner envelope. A cut across the source perpendicular to the jet axis shows that the emission is seen across the source with the redshifted and blueshifted peaks on either side of the source (Fig 8a), similar to that seen in the  $\text{C}^{18}\text{O}$  and  $^{13}\text{CO}$  emission (Paper I) but closer to the source tracing the inner envelope. The blueshifted emission has a peak at  $\sim (-1 \text{ km s}^{-1}, -0\rlap{.}^{\prime\prime}05)$  in the west, while the redshifted emission has a peak at  $\sim (1 \text{ km s}^{-1}, 0\rlap{.}^{\prime\prime}05)$  in the east. This PV structure suggests that the inner envelope is not only rotating around the source but also infalling toward the source with the redshifted emission from the nearside and the blueshifted emission from the farside (Paper I). The emission is optically thick, with the absence of the emission around the systemic velocity. The blueshifted emission is much brighter than the redshifted emission, consistent with a presence of an infall motion (Evans 1999). Note that the redshifted emission in the west at  $\sim (0.7 \text{ km s}^{-1}, -2\rlap{.}^{\prime\prime})$  may arise from the shell. On the other hand, the origin of the  $\text{H}^{13}\text{CO}^+$  emission is unclear and may arise from both the inner envelope and the shell.

The kinematics of the shells can be studied with the cuts across the shells centered at the jet axis. A cut across the shell at  $2\rlap{.}^{\prime\prime}5$  north of the source shows two opposite  $\text{HCO}^+$  crescents at  $\sim \pm 1 \text{ km s}^{-1}$  and one  $\text{H}^{13}\text{CO}^+$  structure around the systemic velocity (Fig. 8b). The two crescents may form the two ends of an elliptical structure connected by the  $\text{H}^{13}\text{CO}^+$  structure, suggesting that the shell there is expanding at  $\sim 1 \text{ km s}^{-1}$ . The  $\text{HCO}^+$  shell is probably optically thick, with the absence of the emission around the systemic velocity. The redshifted emission is much brighter than the blueshifted emission, consistent with a presence of an outflow motion. Cuts across the shell at  $1\rlap{.}^{\prime\prime}25$  north (Fig. 8c) and  $1\rlap{.}^{\prime\prime}25$  south (Fig. 8d) of the source show a hint of rotation with the redshifted emission to the east and the blueshifted emission to the west, similar to that seen in the inner envelope, suggesting that the shell is probably the material extended from the inner envelope. Note that, however, the center of symmetry is

shifted by  $\sim 0\rlap{.}^{\prime\prime}5$  to the east in the north, while  $0\rlap{.}^{\prime\prime}5$  to the west in the south from the jet axis.

### 3.4.3. Temperature, Column density, and Density

In the following, we derive the excitation temperature, column density, and density, assuming optically thin emission and local thermal equilibrium. Note that due to the absorption of the ambient cloud, that part of the emission is optically thick, and that part of the emission is resolved out by the interferometer, the values of the column density and density presented here are lower limits of the true values.

The excitation temperature of the CO emission can be derived from the line ratio of  $\text{CO } J = 3 - 2 / J = 2 - 1$  along the jet axis (Fig. 9a), using the  $\text{CO } J = 2 - 1$  observations from Paper I. Note that, however, since the emission around  $7 \text{ km s}^{-1}$  is resolved out more in  $\text{CO } J = 2 - 1$ , the line ratio there is not properly calculated and appears to be larger than the maximum value of 2.25. In addition, since some of the emission, mostly at high velocity, is too weak to be detected in  $\text{CO } J = 2 - 1$ , the line ratio there also appears to be larger than the maximum value of 2.25. At a given projected distance from the source, the line ratio increases from low velocity to high velocity, suggesting that  $\text{CO } J = 3 - 2$  traces high velocity (and thus jet) better than  $\text{CO } J = 2 - 1$ . The temperature of the shells is found to be  $\sim 20 \text{ K}$  (Fig. 9b). The temperature of the high-velocity emission in the jet is higher and assumed to be 50 K, with a peak brightness temperature found to be  $\sim 35 \text{ K}$  in knot SS. The  $\text{H}_2$  column density can be derived assuming a CO abundance of  $8.5 \times 10^{-5}$  (Frerking et al. 1982). In the jet, it is found to be  $\sim 0.4 \times 10^{21} \text{ cm}^{-2}$  in the continuous structures and  $\sim 1.2 \times 10^{21} \text{ cm}^{-2}$  in knots SS and SN. Therefore, with a diameter of  $\sim 1\rlap{.}^{\prime\prime}$ , the continuous structures has a density of  $5.8 \times 10^4 \text{ cm}^{-3}$ , and knots SS and SN have a density of  $1.7 \times 10^5 \text{ cm}^{-3}$ , similar to that found in the CO jet of HH 211 (Gueth & Guilloteau 1999). On the other hand, the shells are found to have a column density of  $(2 - 7) \times 10^{20} \text{ cm}^{-2}$  and thus a density of  $\sim (0.3 - 1.0) \times 10^5 \text{ cm}^{-3}$ , with a shell thickness of  $\sim 1\rlap{.}^{\prime\prime}$ .

The excitation temperature of the SiO emission has been found to be 50–150 K (Gibb et al. 2004) and is thus assumed to be 100 K here. This temperature, derived at much lower angular resolution, can be considered as the lower limit of the true value. With this temperature, the SiO column density is found to be  $1.5 - 2.5 \times 10^{14} \text{ cm}^{-2}$  toward the bow shocks and knots. The SiO abundance has been found to be  $5 \times 10^{-8}$  (Gibb et al. 2004). With a size  $\lesssim 1\rlap{.}^{\prime\prime}$ , the density is  $\gtrsim (4 - 7) \times 10^5 \text{ cm}^{-3}$ . Note that, since the temperature of the SiO emission could be higher, i.e., 300–500 K as seen in HH 211 (Hirano et al. 2006), the density could be a factor of a few higher.

The excitation temperature of the SO emission can be derived from the line ratio of  $\text{SO } N_J = 8_9 - 7_8 / N_J = 5_6 - 4_5$ , using the  $\text{SO } N_J = 5_6 - 4_5$  observations from Paper I. With a line ratio of  $\sim 1.5$ , the excitation temperature is found to be  $\sim 100 \text{ K}$ , similar to that found in the CepA-East outflows (Codella et al. 2005). The SO column density is found to be  $\sim 8 \times 10^{14} \text{ cm}^{-2}$ . In shock model, the SO abundance is predicted to be  $3 \times 10^{-8} - 6 \times 10^{-7}$  at 100 K (Viti, Natarajan, & Williams 2002). Thus, with a size of  $\sim 1\rlap{.}^{\prime\prime}$ , the density is  $2 \times 10^5 - 4 \times 10^6 \text{ cm}^{-3}$ .

The excitation temperature of the  $\text{HCO}^+$  emission is close to the dust temperature, with a peak brightness temperature found to be  $\sim 41$  K toward the source. Assuming a temperature of 50 K, the  $\text{HCO}^+$  column density is found to be  $\sim 3.2 \times 10^{13} \text{ cm}^{-2}$  toward the source and  $1.8 \times 10^{13} \text{ cm}^{-2}$  toward the shells. The abundance of  $\text{HCO}^+$  is uncertain. It is  $\sim 2 \times 10^{-9}$  in molecular cloud cores (Girart et al. 2000) but greatly enhanced in outflow interacting regions by a factor of 20 with a value of  $4 \times 10^{-8}$  (Hogerheijde et al. 1998; Viti, Natarajan, & Williams 2002). Therefore, with a thickness of  $\sim 1''$ , the density is  $1.2 \times 10^5 - 2.4 \times 10^6 \text{ cm}^{-3}$  toward the source and  $6.5 \times 10^4 - 1.3 \times 10^6 \text{ cm}^{-3}$  toward the shells.

The excitation temperature of the  $\text{H}^{13}\text{CO}^+$  emission is unknown and assumed to be the same as that of the  $\text{HCO}^+$  emission. The  $\text{H}^{13}\text{CO}^+$  column density is found to be  $\sim 6 \times 10^{12} \text{ cm}^{-2}$ . The  $\text{H}^{13}\text{CO}^+$  abundance has been found to be  $\sim 10^{-10}$  in molecular cloud cores (see, e.g., Takakuwa et al. 2003), but is unknown in outflow interacting regions and could be enhanced by a factor of 20, as the  $\text{HCO}^+$  abundance. Thus, the density is  $4 \times 10^5 - 8 \times 10^6 \text{ cm}^{-3}$ , with a thickness of  $\sim 1''$ .

#### 4. DISCUSSION

##### 4.1. Molecular Jet

###### 4.1.1. Shocks: $\text{SiO}$ , $\text{CO}$ , and $\text{H}_2$

$\text{SiO}$  is seen tracing the shocks in the jet, as in HH 211 (Palau et al. 2006). The emission is seen around the bow shocks with a range of velocities, as predicted in the jet-driven bow shock models (see, e.g., Lee et al. 2001). Knots SN and SS are likely unresolved bow shocks, associated with a similar range of velocities.  $\text{H}_2$  emission is also seen associated with them in the Spitzer IRAC 4 (8  $\mu\text{m}$ ) and IRAC 3 (5.8  $\mu\text{m}$ ) images. No  $\text{H}_2$  emission is seen associated with them in the VLT image at 2.12  $\mu\text{m}$  is likely because of the severe dust extinction toward them at that wavelength. The spectra toward bow shocks NK4, SK2 and SK4 and knot SS are asymmetric: steep toward the highest velocities with a wing pointing toward the lowest velocities (Fig. 10), also as predicted in the shock model in which the  $\text{SiO}$  abundance is enhanced more at higher shock velocity (Schilke et al. 1997). It is believed that  $\text{SiO}$  abundance is enhanced as a consequence of grain sputtering or grain-grain collisions releasing Si-bearing material into the gas phase, which reacts rapidly with O-bearing species (e.g.,  $\text{O}_2$  and  $\text{OH}$ ) to form  $\text{SiO}$  (Schilke et al. 1997; Caselli et al. 1997). The emission is consistent with its production in C-type shocks, with a total velocity range of  $\sim 20 \text{ km s}^{-1}$  (see Fig. 10), similar to that found to produce the observed  $\text{SiO}$  column densities in molecular outflows (Schilke et al. 1997). The C-type shocks have also been argued to produce the high shock velocity gas seen in  $\text{H}_2$  (Zinnecker, McCaughrean, & Rayner 1998). The  $\text{SiO}$  emission, with the derived density orders of magnitude lower than the critical density, may arise from “thinner” regions, as in thin shock fronts.

$\text{SiO}$  may trace different shock conditions from  $\text{H}_2$ . As mentioned, although  $\text{H}_2$  emission is bright around bow shocks NK1 and SK1,  $\text{SiO}$  emission is faint around them, and is faintest around the former. In  $\text{H}_2$ , the FWHM velocity widths toward the bow shocks were found to be 9 (NK7), 6 (NK4), 12 (NK2), 31 (NK1), 21 (SK1), and 6

(SK2)  $\text{km s}^{-1}$  (Davis et al. 2000; Takami et al. 2006), indicating that the shock is much stronger for bow shocks NK1 and SK1, and is strongest for the former. Thus, it is possible that  $\text{SiO}$  around bow shocks NK1 and SK1 is mostly destroyed by the shocks through reactions such as  $\text{SiO} + \text{OH} \rightarrow \text{SiO}_2 + \text{H}$  (see, e.g., Schilke et al. 1997). On the other hand,  $\text{SiO}$  and  $\text{H}_2$  are known to trace different physical conditions, with  $\text{SiO}$  ( $T_{\text{ex}} \sim 100 \text{ K}$ ,  $n_{\text{cr}} \sim 10^8 \text{ cm}^{-3}$ ) tracing much cooler but much denser gas than  $\text{H}_2$  ( $T_{\text{ex}} \sim 2000 \text{ K}$ ,  $n_{\text{cr}} \sim 10^6 \text{ cm}^{-3}$  for  $\text{H}_2$ - $\text{H}_2$  collision). Thus, it is also possible that although gas-phase  $\text{SiO}$  is being produced, the density there is not high enough to produce bright collisionally excited  $\text{SiO}$  emission.  $\text{CO}$  emission ( $T_{\text{ex}} \sim 50 \text{ K}$ ,  $n_{\text{cr}} \sim 4 \times 10^4 \text{ cm}^{-3}$ ), which traces cooler and less dense gas than  $\text{SiO}$  emission, is seen around there, also supporting this possibility. This possibility may apply as well to weak bow shocks such as NK6, NK7, and SK5. For those weak bow shocks, however, it is also possible that  $\text{SiO}$  there is depleted back onto grains in the postshock gas.

The density in the bow shocks is expected to decrease with the distance from the source due to the sideways ejection of the shocked material and the possible thermal expansion of the jet. The fact that the  $\text{CO}$  emission decreases with the distance from the source (see Fig. 10) also supports this possibility. However, due to the shock enhancement, the  $\text{SiO}$  emission is brightest around bow shocks NK4 and SK2.

$\text{CO}$  emission is also seen tracing the shocks in the jet. For those bow shocks, e.g., NK4 and SK4, where  $\text{CO}$  and  $\text{SiO}$  emission are coincident, the velocity dispersion is smaller in  $\text{CO}$  than  $\text{SiO}$ , suggesting that  $\text{CO}$  traces weaker shock than  $\text{SiO}$ . It is likely because  $\text{CO}$  traces cooler and less dense gas than  $\text{SiO}$ , and thus further away from the bow tip where the shock velocity is lower.

###### 4.1.2. Inclination

The jet inclination,  $i$ , can be estimated from the mean velocity of the  $\text{SiO}$  emission,  $v_m$ , with  $i = \sin^{-1}(v_m/v_j)$ , where  $v_j$  is the jet velocity. The northern component and southern component of the jet, however, may have different inclinations because of their different mean velocities. Assuming the same jet velocity, the northern component and southern component of the jet have an inclination of  $\sim 6.3^\circ(100 \text{ km s}^{-1}/v_j)$  and  $4.0^\circ(100 \text{ km s}^{-1}/v_j)$ , respectively, in agreement with that found from the water masers (Claussen et al. 1998). Note that, knots SS and SN may have lower inclinations, because of their lower mean velocities.

###### 4.1.3. Mass-loss rate

Continuous structures between the bow shocks may trace the “intrinsic” jet itself, allowing us to estimate the mass-loss rate of the jet, which is given by

$$\dot{M}_j \sim n_c \frac{\pi d_c^2}{4} v_j m_{\text{H}_2} \quad (1)$$

where  $n_c$  and  $d_c$  are the number density and the diameter of the continuous structures. With  $n_c \sim 5.8 \times 10^4 \text{ cm}^{-3}$ ,  $d_c \sim 460 \text{ AU}$ , (i.e.,  $1''$ ), and  $v_j = 100 - 200 \text{ km s}^{-1}$ , the mass-loss rate is  $(1 - 2) \times 10^{-6} M_{\odot} \text{ yr}^{-1}$ , about 15%–30% of the infall rate derived from the envelope (Paper I).

#### 4.1.4. Episodic nature

In the inner part of the jet, a chain of bow shocks are seen with a semiperiodic spacing of  $\sim 3''$ . Between the bow shocks, the continuous structures are seen probably with the velocity increasing periodically from one bow shock to the next, suggesting that the jet velocity varies periodically with time and is highest at the far ends of the continuous structures. These are consistent with a pulsed (i.e., episodic) jet model with a periodical velocity variation, in which a chain of bow shocks are formed as the fast-moving jet material impacts on the slow-moving jet material (see, e.g., Suttner et al. 1997; Lee et al. 2001). The jetlike SO emission around the source, where the velocity probably has not steeped into shock, may show intrinsically how the velocity varies with time. Observations at higher angular resolution are needed to resolve it.

The period of the velocity variation, which can be estimated by dividing the semiperiodic spacing between the bow shocks by the jet velocity, is found to be  $P \sim 65(100 \text{ km s}^{-1}/v_j) \text{ yr}$ . The jet is believed to be launched from an accretion disk around the source. The periodic velocity variation may be due to periodic perturbation of the accretion disk in an eccentric binary system; in this case the period of the velocity variation is equal to the orbital period of the binary and the separation of the binary is given by

$$a = \left( \frac{GMP^2}{4\pi^2} \right)^{1/3} \quad (2)$$

where  $M$  is the total mass of the binary. With  $M \sim 0.15 M_\odot$  (Paper I) and  $P = 65 \text{ yr}$ , we have  $a \sim 8 \text{ AU}$  (i.e.,  $0''.02$ ), similar to that estimated in HH 34 (Reipurth et al. 2002). A binary with this separation, however, would be unresolved in our observations. The periodic variation may also be due to FU Ori like events as the disk builds up mass from the envelope then dumps it onto the protostar in a burst.

#### 4.1.5. Precessing

The jet itself may be slightly precessing as the jetlike SO emission shows a slight S-shaped symmetry about the source. The fact that the continuous structures seen in H<sub>2</sub> and CO are sinuous also supports this possibility. The angle of precession can be assumed to be the angle subtended by the continuous structures and is found to be  $\lesssim 2^\circ$ . Since the continuous structures may show a full cycle between bow shocks SK1 and SK2, and between bow shocks NK1 and NK2, the period of the precession is probably similar to that of the velocity variation, suggesting that the precession is also due to a binary system. A slight S-shaped symmetry is also seen in other jets, e.g., HH 34, and is generally ascribed to the tidal effects of the companion star on the direction of the jet axis (Reipurth et al. 2002). However, it is also possible that the slight precession is due to kink instability in the jet (Todo et al. 1993).

#### 4.1.6. Bending

The inner part of the jet is bent by  $\sim 1^\circ$  to the west. Similar jet bending is also seen in HH 211 (Gueth & Guilloteau 1999). It has been proposed that a jet can be bent (or deflected) by the dynamical pressure of the ambient medium (Fendt & Zinnecker 1998). However,

it is not clear how the ambient medium can be communicated to the highly supersonic jet.

The bending could be due to motion of the jet source in a binary system (Fendt & Zinnecker 1998). In this case, a binary system with a minimum separation of  $\sim 0''.5$  (or 230 AU), which is the lower limit set by the half displacement of bow shocks NB1/2 and SB1/2 from the original axis, is required. However, no binary companion has been detected yet. It is possible that the bending is due to Lorentz force on the magnetic jet (Fendt & Zinnecker 1998). It is also possible that the jet can appear to be bent just due to the motion of the star/disk system, i.e. the jet is originating from different positions as a function of time due to the star's peculiar velocity.

#### 4.1.7. Rotation?

In theoretical jet-launching models, the jet is expected to be rotating, carrying away angular momentum from the infalling envelope and the accretion disk. The far end of the southern component of the SO jetlike structure, which is at a beam size ( $\sim 1''$ ) away from the source, is likely far enough from the possible disk contamination around the source and thus can be used to study the jet rotation. However, no clear velocity gradient is seen across it (Fig. 11a). Knots SS and SN are the shocks closest to the source and can also be used to study the jet rotation. Although no clear velocity gradient is seen across knot SS (Fig. 11b), a velocity gradient is seen across knot SN (Fig. 11c) with the redshifted emission to the east and the blueshifted emission to the west, similar to that seen in the envelope. Thus, jet rotation may be seen in our observations. Observations at higher angular resolution are needed to confirm this.

### 4.2. Molecular Outflow Shells

Outflow shells are seen in CO  $J = 3 - 2$  surrounding the jet extending to the north and south from the diffuse nebulae that trace the outflow cavity walls (MZAML02), similar to that seen in CO  $J = 2 - 1$  (Paper I). However, the shells are asymmetric in CO  $J = 3 - 2$ , with the northern shell bright in the west and southern shell bright in the east. Since CO  $J = 3 - 2$  traces warmer material and thus more recent outflow interactions than CO  $J = 2 - 1$ , this asymmetry indicates that the recent outflow interactions are asymmetric. This can be explained if the jet axis has rotated in the clockwise direction recently, as suspected from the morphology of the H<sub>2</sub> jet (see §3.2).

Around the source, internal outflow shells are seen in CO and HCO<sup>+</sup> associated with, e.g., bow shocks SK1 and NK1. They probably trace the material squirted out from the bow shocks, as in pulsed jet model (see, e.g., Suttner et al. 1997; Lee et al. 2001). The shells are asymmetric, with the northern shell bright in the east and the southern shell bright in the west. This is expected if the shells are produced by the slight S-shaped jetlike SO structure. The bases of the HCO<sup>+</sup> shells, which are seen with a hint of rotation, however, are probably consisted mainly of the material extended from the inner envelope and even the possible disk. The bases are also seen in H<sup>13</sup>CO<sup>+</sup> and continuum, probably tracing the dense material extended from around the same regions.

These internal outflow bases may trace the material entrained from the inner envelope by the jet. However, in the

currently existing jet simulations (see, e.g., Suttner et al. 1997; Downes & Ray 1999; Lee et al. 2001; Raga et al. 2004), no internal outflow bases have been seen because the jet is protected by a slower sheath shock from continued interaction with the ambient material at its bases. It is possible that these internal outflow bases trace the material directly launched from the inner envelope (and even the possible disk) around the jet and then swept up by the internal bow shocks, e.g., NK1 and SK1, of the jet. Further simulations are needed to study this.

#### 4.3. Wide-angle wind component?

The jet itself is clearly highly collimated, yet the diffuse nebulae clearly show the classic bipolar parabolic shape with a wide opening angle. This may suggest that an unseen wide-angle wind component is there to produce the diffuse nebulae, so that the jet is only a dense component of a wider wind. However, as seen in Figure 2a, the jet produces a chain of bow shocks with the interacting surface growing with the distance from the source, and thus producing a few prominent bow shocks with much bigger interacting surfaces than the jet itself. Through these bow shocks, a jet may be able to produce wide-opening outflow bases such as the diffuse nebulae. Detailed modelings are needed to check this.

#### 4.4. Molecular Envelope and Disk?

The  $\text{HCO}^+$  emission around the source may arise from the inner part of a dynamically infalling envelope with rotation, showing a kinematics similar to that seen in the  $\text{C}^{18}\text{O}$  and  $^{13}\text{CO}$  emission in Paper I, but closer to the source. As argued in Paper I, a compact rotationally supported disk with a radius of  $\sim 74$  AU (or  $0''.16$ ) is expected to be formed within the inner part of the envelope. In order to study it, the PV diagrams of  $\text{HCO}^+$ ,  $\text{CO}$ , and  $\text{SO}$  emission cut across the source are compared with a Keplerian rotation law (with a source mass of  $0.15 M_\odot$ , Paper I) and a rotation law with a constant specific angular momentum (Fig. 12). In the diagrams, the large-scale emission structures are excluded (see §2), in order to study the inner regions. Note that the comparison could be affected by the missing flux around the systemic velocity. Rotation is clearly seen within 100 AU from the source in  $\text{CO}$  and  $\text{HCO}^+$ , with the redshifted emission on the east and the blueshifted emission on the west. The  $\text{SO}$  emission may have two components, with the low velocity ( $\lesssim 2 \text{ km s}^{-1}$  from the systemic velocity) from the rotation and the high

velocity from the jet. The PV structures seem better fitted by the rotation law with a constant specific angular momentum, indicating that the emission within 100 AU from the source probably is still from the inner part of a dynamically infalling envelope with rotation rather than a rotationally supported disk. The rotation may change to Keplerian in the innermost region. Observations at higher angular resolution and detailed modeling are both needed to check this.

#### 5. CONCLUSIONS

We have mapped the protostellar jet HH 212 in  $850 \mu\text{m}$  continuum,  $\text{SiO } J = 8-7$ ,  $\text{CO } J = 3-2$ ,  $\text{SO } N_J = 8_9-7_8$ ,  $\text{HCO}^+ J = 4-3$ , and  $\text{H}^{13}\text{CO}^+ J = 4-3$  emission. Thermal dust emission is seen in continuum around the source IRAS 05413-0104, mainly arising from an inner envelope and a possible disk. The inner envelope is also seen with rotation in  $\text{CO}$ ,  $\text{HCO}^+$ , and probably  $\text{SO}$ . The structure is unresolved but likely to be flattened perpendicular to the jet axis, as seen in the CLEAN component map. Like  $\text{H}_2$  emission,  $\text{CO}$  and  $\text{SiO}$  emission are seen along the jet axis but extending closer to the source, tracing the bow shocks with a broad range of velocities and the continuous structures in between.  $\text{SO}$  emission is seen only around the source, forming a jetlike structure extending along the jet axis from the source, likely tracing the jet near the launching region. The jet is episodic and bending. It may also be slightly precessing as the jetlike  $\text{SO}$  structure shows a slight S-shaped symmetry about the source. A hint of jet rotation is also seen across the jet axis. Internal outflow shells are seen in  $\text{CO}$  and  $\text{HCO}^+$ , associated with the bow shocks in the inner part of the jet. The bases of the  $\text{HCO}^+$  shells are seen with a hint of rotation similar to that seen in the inner envelope, probably consisted mainly of the material extended from the inner envelope and even the possible disk. The bases of the outflow shells are also seen in  $\text{H}^{13}\text{CO}^+$  and even the continuum, probably tracing the dense material extended from around the same regions. Outflow shells are also seen in  $\text{CO}$  surrounding the jet extending out from the  $\text{H}_2$  nebulae. They are probably internal outflow shells associated with the bow shocks further down the jet axis.

We thank the anonymous referee for insightful comments. We thank the SMA staff for their efforts in running and maintaining the array. H.B. acknowledges financial support by the Emmy-Noether-Program of the Deutsche Forschungsgemeinschaft (DFG, grant BE2578).

#### REFERENCES

Beckwith, S. V. W., Sargent, A. I., Chini, R. S., & Guesten, R. 1990, *AJ*, 99, 924  
 Caselli, P., Hartquist, T. W., & Havnes, O. 1997, *A&A*, 322, 296  
 Chapman, N. L., Mundy, L. G., Lee, C.-F., & White, S. M. 2002, *Bulletin of the American Astronomical Society*, 34, 1133  
 Claussen, M. J., Marvel., K.B., Wootten, A., Wilking, B.A. 1998, *ApJL*, 507, L79  
 Codella, C., Bachiller, R., Benedettini, M., Caselli, P., Viti, S., & Wakelam, V. 2005, *MNRAS*, 361, 244  
 Davis, C. J., Berndsen, A., Smith, M. D., Chrysostomou, A., & Hobson, J. 2000, *MNRAS*, 314, 241  
 Downes, T. P., Ray, T. P. 1999, *A&A*, 345, 977  
 Evans, N. J. 1999, *ARA&A*, 37, 311  
 Fendt, C., & Zinnecker, H. 1998, *A&A*, 334, 750  
 Frerking, M. A., Langer, W. D., & Wilson, R. W. 1982, *ApJ*, 262, 590  
 Galván-Madrid, R., Avila, R., & Rodríguez, L. F. 2004, *Revista Mexicana de Astronomía y Astrofísica*, 40, 31  
 Gibb, A. G., Richer, J. S., Chandler, C. J., & Davis, C. J. 2004, *ApJ*, 603, 198  
 Girart, J. M., Estalella, R., Ho, P. T. P., & Rudolph, A. L. 2000, *ApJ*, 539, 763  
 Gueth, F., & Guilloteau, S. 1999, *A&A*, 343, 571  
 Hartigan, P., Bally, J., Reipurth, B., & Morse, J. A. 2000, *Protostars and Planets IV*, 841  
 Hirano, N., Liu, S.-Y., Shang, H., Ho, P. T. P., Huang, H.-C., Kuan, Y.-J., McCaughrean, M. J., & Zhang, Q. 2006, *ApJ*, 636, L141  
 Ho, P. T. P., Moran, J. M., & Lo, K. Y. 2004, *ApJ*, 616, L1

Hogerheijde, M. R., van Dishoeck, E. F., Blake, G. A., & van Langevelde, H. J. 1998, ApJ, 502, 315

Jørgensen, J. K., Bourke, T.L., Myers, P.C. Di Francesco, J., Lee, C.-F., Ohashi, N., Schöier, F. L., Takakuwa, S., van Dishoeck, E. F., Wilner, D.J., & Zhang, Q. 2006, ApJ, *submitted*.

Konigl, A., & Pudritz, R. E. 2000, Protostars and Planets IV, 759

Lee, C.-F., Mundy, L.G., Reipurth, B., Ostriker, E.C., & Stone, J.M. 2000, ApJ, 542, 925

Lee, C.-F., Stone, J. M., Ostriker, E. C., & Mundy, L. G. 2001, ApJ, 557, 429

Lee, C.-F., Ho, P. T. P., Beuther, H., Bourke, T. L., Zhang, Q., Hirano, N., & Shang, H. 2006, ApJ, 639, 292

McCaughrean, M., Zinnecker, H., Andersen, M., Meeus, G., & Lodieu, N. 2002, The Messenger, 109, 28 (MZAML02)

Palau, A., et al. 2006, ApJ, 636, L137

Raga, A. C., Noriega-Crespo, A., González, R. F., & Velázquez, P. F. 2004, ApJS, 154, 346

Reipurth, B., Heathcote, S., Morse, J., Hartigan, P., & Bally, J. 2002, AJ, 123, 362

Schilke, P., Walmsley, C. M., Pineau des Forets, G., & Flower, D. R. 1997, A&A, 321, 293

Shu, F.H., Najita, J., Shang, H., & Li, Z. -Y. 2000, in Protostars and Planets IV, ed. V. Mannings, A. P. Boss & S. S. Russell (Tucson: University of Arizona Press), 789

Suttner, G., Smith, M. D., Yorke, H. W. & Zinnecker, H. 1997, A&A, 318, 595

Takakuwa, S., Kamazaki, T., Saito, M., & Hirano, N. 2003, ApJ, 584, 818

Takami, M., Takakuwa, S., Momose, M., Hayashi, M., Davis, C., Pyo, T.-S., Nishikawa, T., & Kohno, K. 2006, PASJ, ??

Todo, Y., Uchida, Y., Sato, T., & Rosner, R. 1993, ApJ, 403, 164

Viti, S., Natarajan, S., & Williams, D. A. 2002, MNRAS, 336, 797

Zinnecker, H., McCaughrean, M. J. & Rayner, J. T. 1998, Nature, 394, 862

Zinnecker, H. , Bastien, P. , Arcoragi, J. -P. & Yorke, H. W. 1992, A&A, 265, 726

TABLE 1  
LINE PROPERTIES

Line	Frequency (GHz)	$E_{\text{up}}$ (K)	$n_{\text{cr}}(50\text{-}100 \text{ K})$ (cm $^{-3}$ )
SiO $J = 8 - 7$	347.330631	75.0	$1.1 \times 10^8$
SO $N_J = 8_9 - 7_8$	346.528481	78.8	$1.4 \times 10^7$
CO $J = 3 - 2$	345.795991	33.2	$3.6 \times 10^4$
HCO $^+$ $J = 4 - 3$	356.734288	42.8	$9.0 \times 10^6$
H $^{13}$ CO $^+$ $J = 4 - 3$	346.998338	41.6	$8.1 \times 10^6$

$n_{\text{cr}}$ : Critical density of molecular hydrogen.

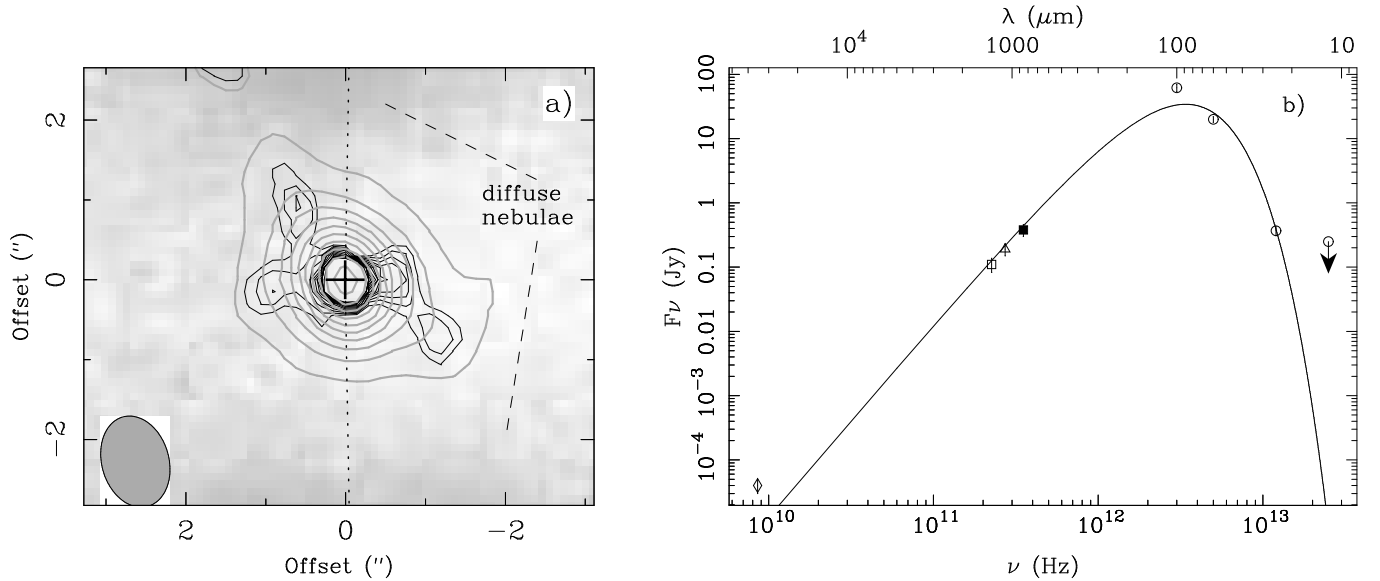


FIG. 1.— (a) 850  $\mu\text{m}$  continuum contours plotted on top of the H<sub>2</sub> image adopted from MZAML02. Note that the image has been rotated by 22.5° clockwise. Gray contours are from the restored map with a synthesized beam of  $1.^{\prime\prime}16 \times 0.^{\prime\prime}84$ , going from 4 to 40  $\sigma$  with a step of 4  $\sigma$ , where  $\sigma = 5 \text{ mJy beam}^{-1}$ . Black contours are from the CLEAN component map. The cross marks the source position. (b) A single-temperature fit to the spectral energy distribution of the continuum source (see text for detail). The squares are from our SMA observations, with the open one from Paper I and the filled one from this paper. The open circles, triangle, and diamond are from the IRAS, JCMT (Zinnecker et al. 1992), and VLA (Galván-Madrid et al. 2004) observations, respectively.

FIG. 2.— (a) The H<sub>2</sub> image adopted from MZAML02. The ellipse outlines the observed region in our observations. The dotted lines indicate the jet axes. The cross marks the source position. (b) The H<sub>2</sub> image rotated by 22.5° clockwise. (c) SiO (integrated from -21.1 to 16.0  $\text{km s}^{-1}$ ) contours plotted on top of the H<sub>2</sub> image. The contours go from 3 to 21  $\sigma$  with a step of 2  $\sigma$ , where  $\sigma = 0.58 \text{ Jy beam}^{-1} \text{ km s}^{-1}$ . (d) High-velocity CO (integrated from -18.4 to -7.1 and from 3.4 to 13.3  $\text{km s}^{-1}$ ) contours plotted on top of the H<sub>2</sub> image. The contours go from 3 to 21  $\sigma$  with a step of 3  $\sigma$ , where  $\sigma = 0.38 \text{ Jy beam}^{-1} \text{ km s}^{-1}$ . The synthesized beams are  $0.^{\prime\prime}96 \times 0.^{\prime\prime}69$  and  $1.^{\prime\prime}16 \times 0.^{\prime\prime}84$ , respectively, for the SiO and CO emission.

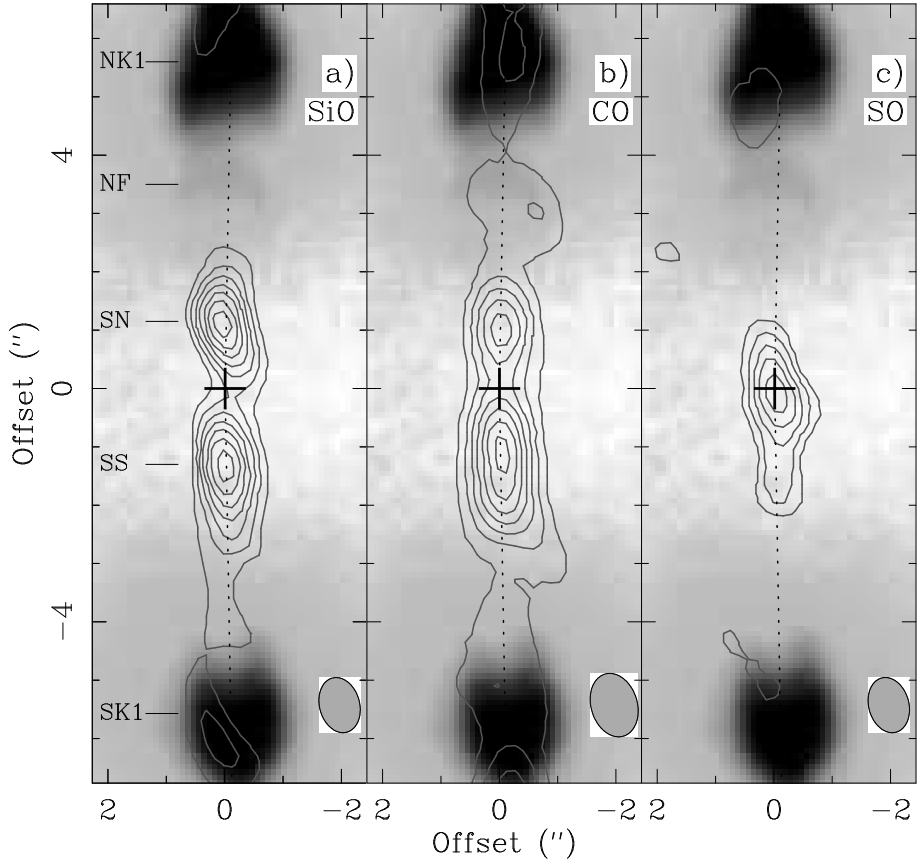


FIG. 3.— (a) SiO, (b) High-velocity CO, and (c) SO contours on top of the H<sub>2</sub> image near the source. The SiO and CO contour levels are the same as those in Fig. 2c and 2d, respectively. The SO (integrated from -11.8 to 11.1 km s<sup>-1</sup>) contours go from 2 to 10  $\sigma$  with a step of 2  $\sigma$ , where  $\sigma = 0.45$  Jy beam<sup>-1</sup> km s<sup>-1</sup>. The synthesized beams are 0''.96  $\times$  0''.69 for the SiO and SO emission and 1''.16  $\times$  0''.84 for the CO emission.

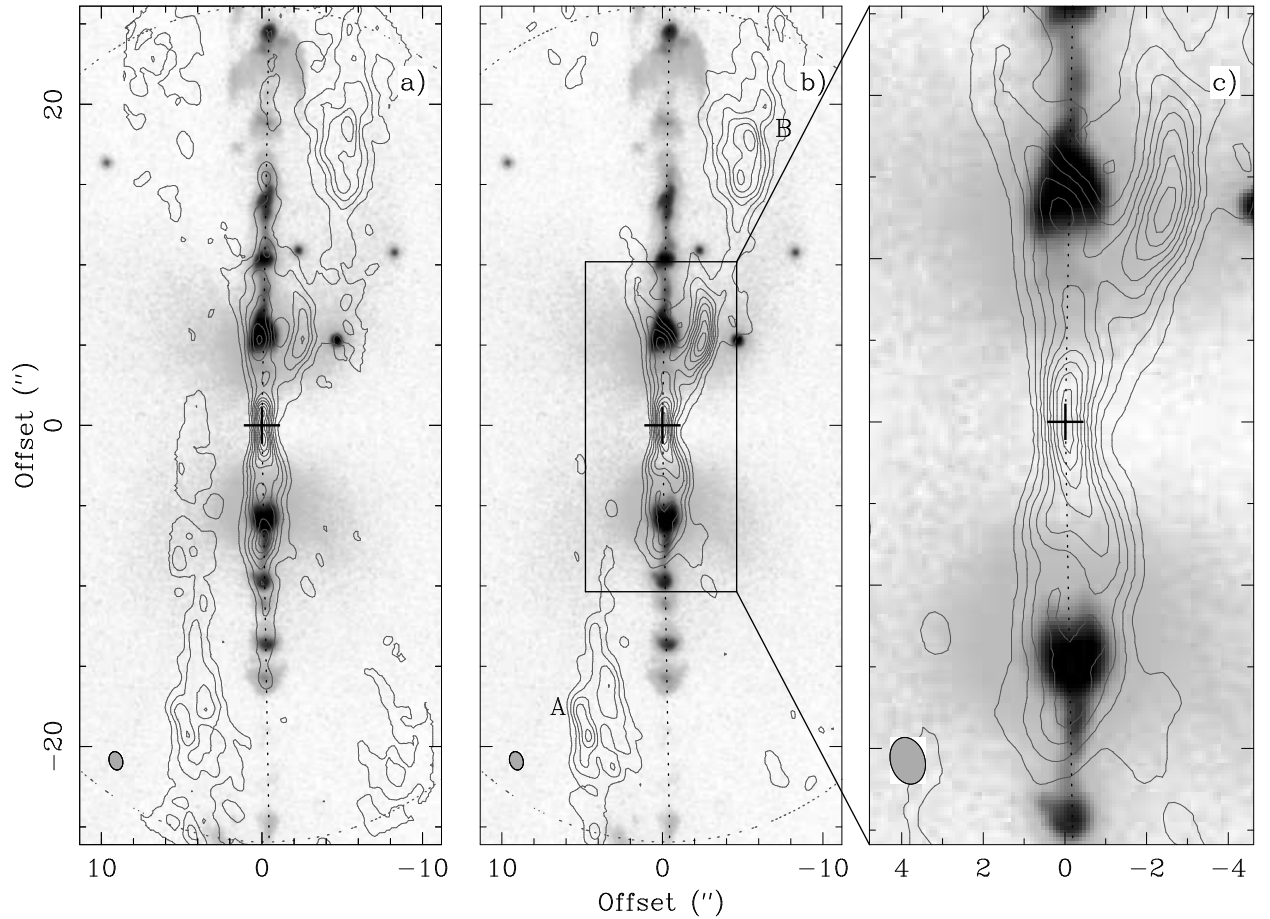


FIG. 4.— CO contours plotted on top of the H<sub>2</sub> image. The synthesized beams all have a size of  $1.^{\prime\prime}16 \times 0.^{\prime\prime}84$ . (a) shows the total CO emission integrated from  $-18.4$  to  $13.3$  km s $^{-1}$ . The contours go from  $4$  to  $36 \sigma$  with a step of  $4 \sigma$ , where  $\sigma = 0.55$  Jy beam $^{-1}$  km s $^{-1}$ . (b) and (c) show the low-velocity CO emission integrated from  $-4.0$  to  $3.1$  km s $^{-1}$ . The contours go from  $5$  to  $45 \sigma$  with a step of  $5 \sigma$ , where  $\sigma = 0.24$  Jy beam $^{-1}$  km s $^{-1}$ .

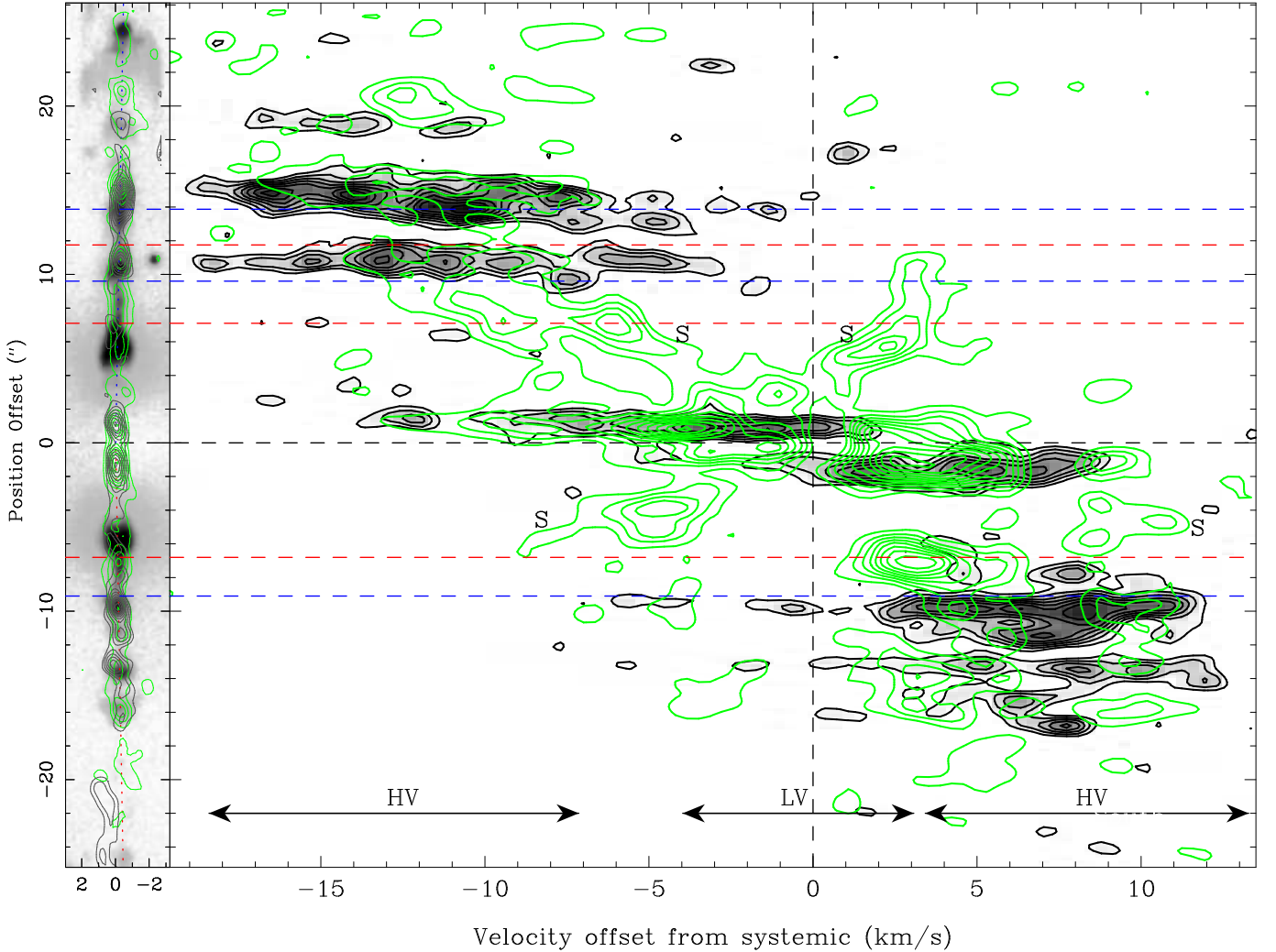


FIG. 5.— PV diagrams of the SiO and CO emission cut along the jet axis with a width of  $0.^{\circ}9$ . (a) SiO (gray) and high-velocity CO (green) contours on top of the H<sub>2</sub> image. (b) PV diagrams of the SiO (black contours with image) and CO (green contours) emission. Here, HV and LV denote the high-velocity and low-velocity ranges, respectively, for the CO emission. The red and blue dashed lines mark the near and far ends of the continuous structures.

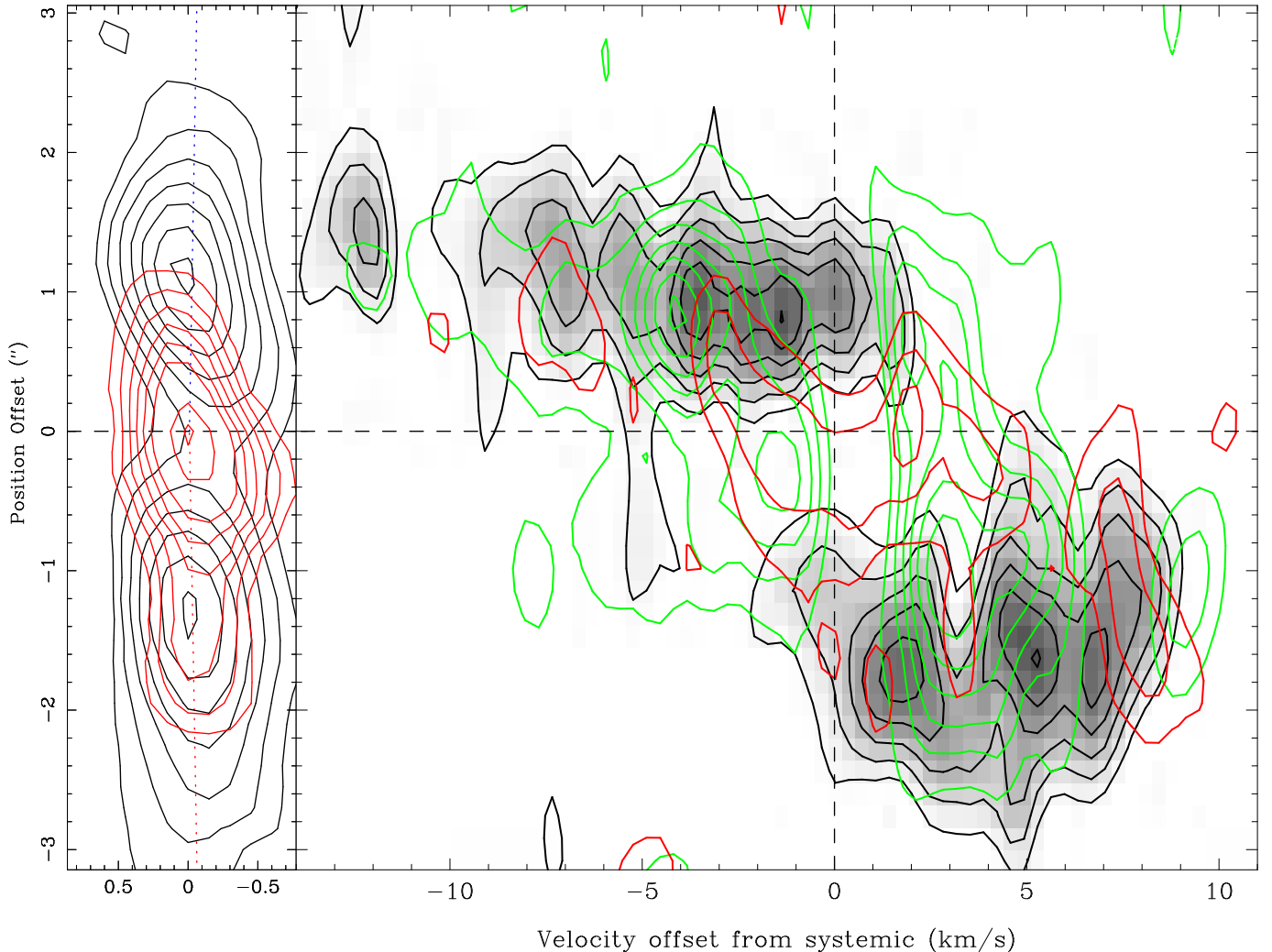


FIG. 6.— PV diagrams of the SiO, CO, and SO emission cut along the jet axis with a width of  $0.^{\prime\prime}9$ . (a) SiO (black) and SO (red) contours. (b) PV diagrams of the SiO (black contours with image), CO (green contours), and SO (red contours) emission.

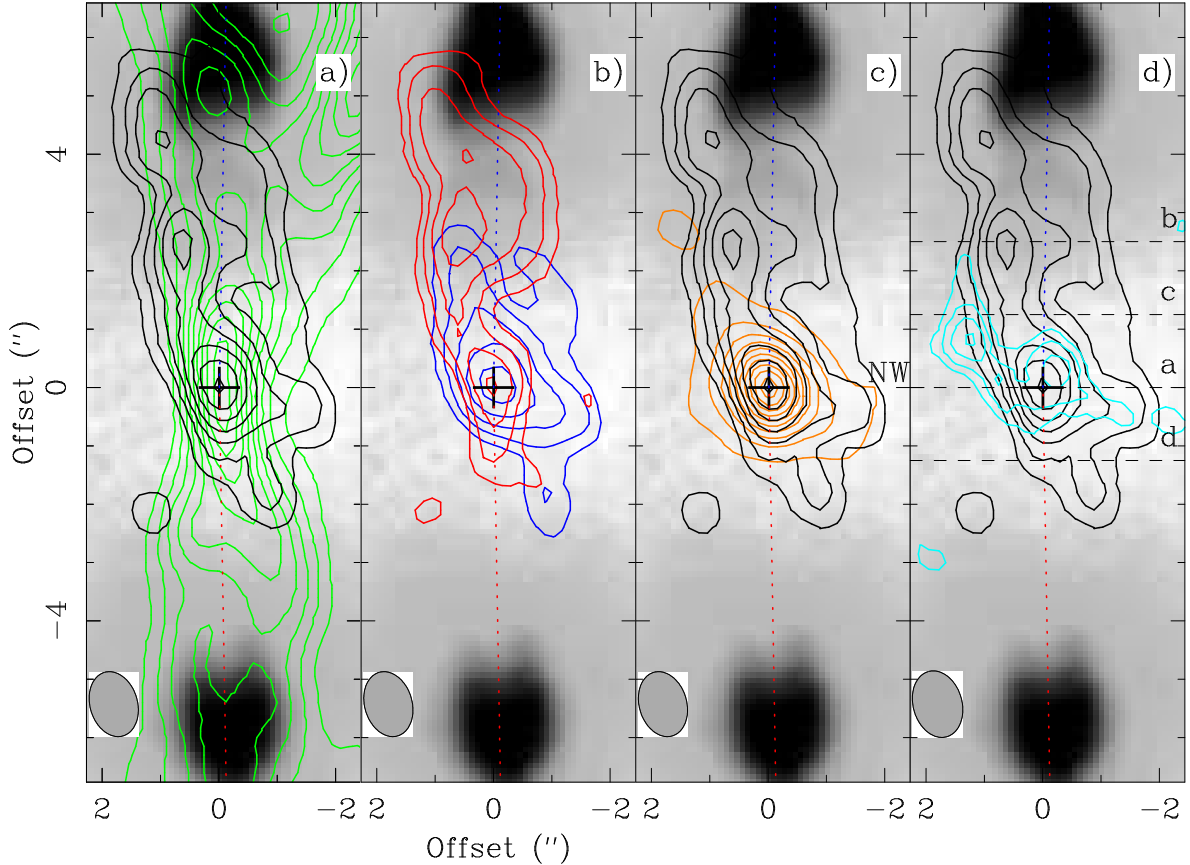


FIG. 7.—  $\text{HCO}^+$ , continuum, and  $\text{H}^{13}\text{CO}^+$  contours plotted on top of the  $\text{H}_2$  image. The synthesized beams all have a size of  $1''\text{16} \times 0''\text{84}$ . (a)  $\text{HCO}^+$  (black, integrated from  $-2.5$  to  $2.5 \text{ km s}^{-1}$ ) and low-velocity CO (green) contours. The  $\text{HCO}^+$  contours go from  $3$  to  $15 \sigma$  with a step of  $2 \sigma$ , where  $\sigma = 0.32 \text{ Jy beam}^{-1} \text{ km s}^{-1}$ . (b) Blueshifted (integrated from  $-2.5$  to  $0 \text{ km s}^{-1}$ ) and redshifted (integrated from  $0$  to  $2.5 \text{ km s}^{-1}$ )  $\text{HCO}^+$  emission, with the contours from  $3$  to  $11$  and  $3$  to  $9 \sigma$ , respectively, with a step of  $2 \sigma$ , where  $\sigma = 0.23 \text{ Jy beam}^{-1} \text{ km s}^{-1}$ . (c)  $\text{HCO}^+$  (black) and continuum (orange) contours. (d)  $\text{HCO}^+$  (black) and  $\text{H}^{13}\text{CO}^+$  (cyan, integrated from  $-1.7$  to  $2.5 \text{ km s}^{-1}$ ) contours. The  $\text{H}^{13}\text{CO}^+$  contours go from  $3$  to  $6 \sigma$  with a step of  $1 \sigma$ , where  $\sigma = 0.20 \text{ Jy beam}^{-1} \text{ km s}^{-1}$ . The horizontal dashed lines indicate the cuts for the PV diagrams in Fig. 8.

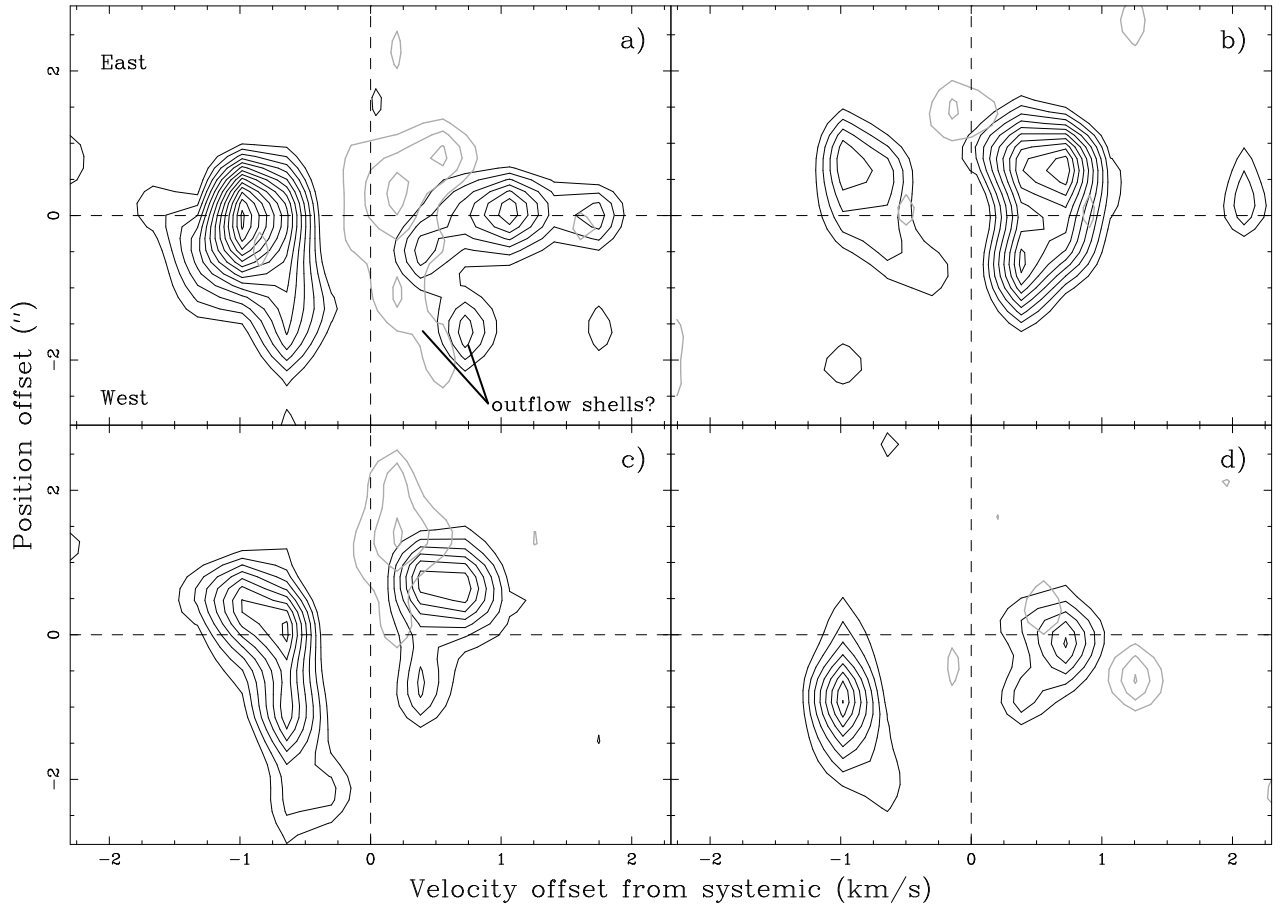


FIG. 8.— PV diagrams of the  $\text{HCO}^+$  (black) and  $\text{H}^{13}\text{CO}^+$  (gray) emission cut across the jet axis, with the cuts shown in Fig 7d. (a) A cut centered at the source. Cuts centered at (b)  $2.5''$  to the north, (c)  $1.25''$  to the north, and (d)  $1.25''$  to the south, respectively, of the source.

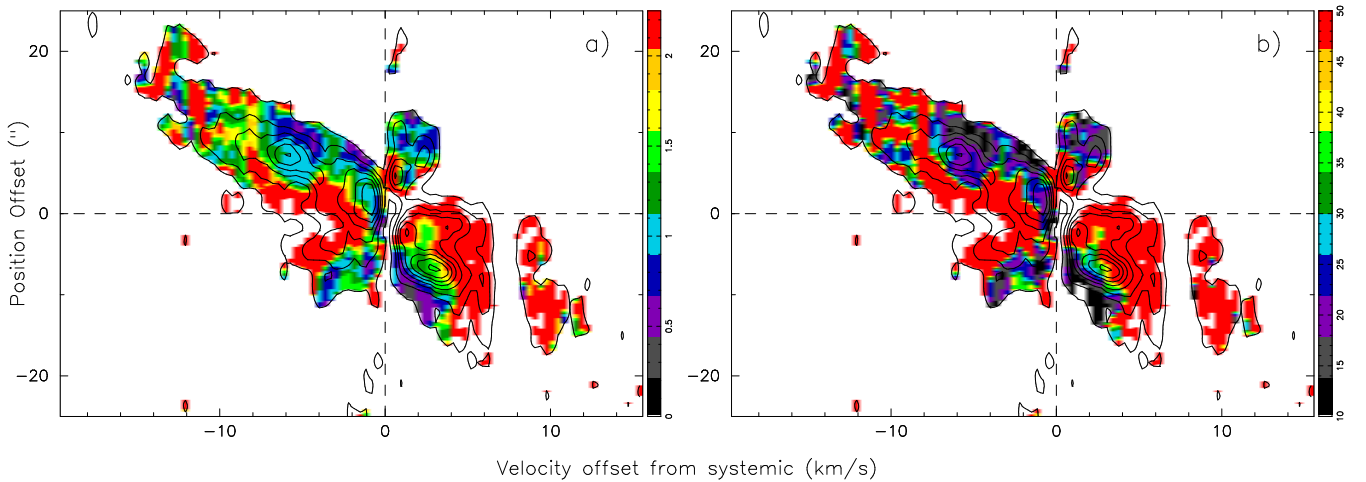


FIG. 9.— (a) Line ratio of  $\text{CO } J = 3 - 2 / J = 2 - 1$  smoothed to the angular resolution in the  $\text{CO } J = 2 - 1$  observations, which is  $\sim 2.5''$ . (b) Excitation temperature derived from the line ratio. The black contours in these two panels show the PV diagram of the  $\text{CO } J = 3 - 2$  emission cut along the jet axis, smoothed to the resolution of the  $\text{CO } J = 2 - 1$  observations.

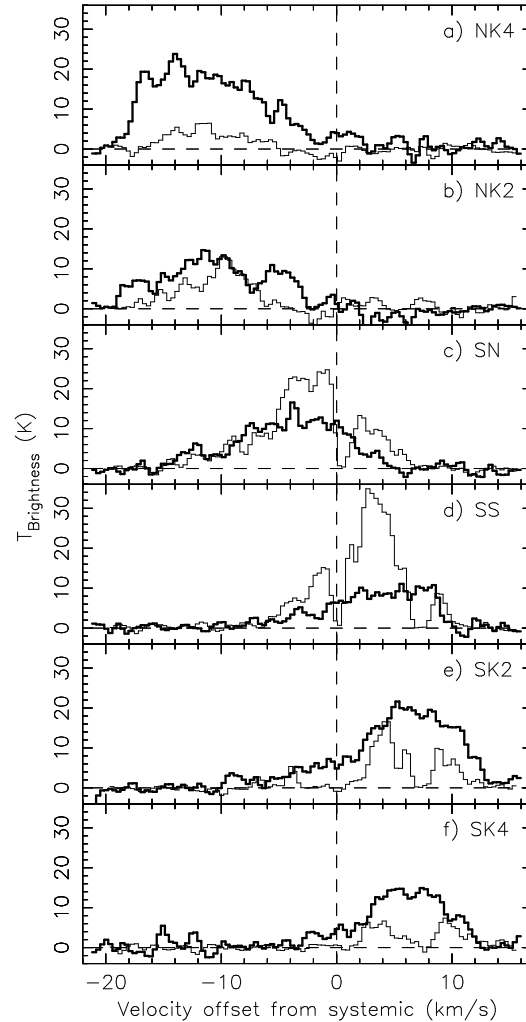


FIG. 10.— SiO (thick lines) and CO (thin lines) spectra toward the bow shocks and knots.

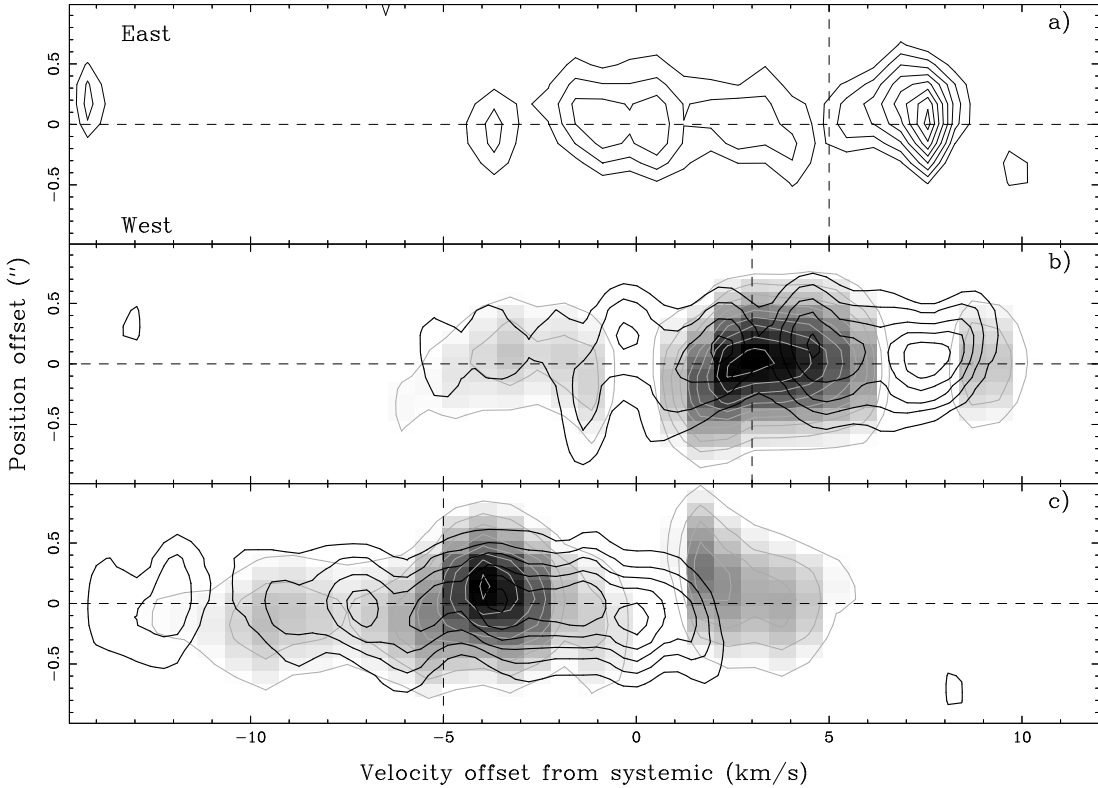


FIG. 11.— PV diagrams with cuts across (a) the southern component of the SO jetlike structure, (b) knot SS, and (c) knot SN. The cuts have a width of  $0.15''$ . The dashed vertical lines indicate the possible jet central velocities for the cuts. In (b) and (c), the black contours are from the SiO emission and the gray-scale image with gray contours is from the CO emission.

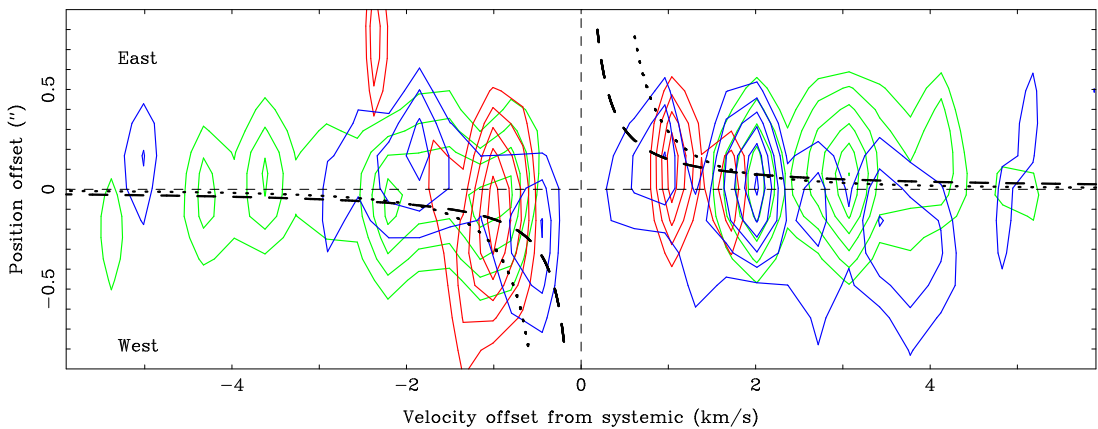


FIG. 12.— PV diagrams of CO (green), HCO<sup>+</sup> (red), and SO (blue) emission cut across the source. The dotted curves are calculated assuming a Keplerian rotation with a source mass of  $0.15 M_{\odot}$ . The dashed curves are calculated assuming a constant specific angular momentum with  $v_{\text{rot}} = \frac{0.15}{d} \text{ km s}^{-1}$ , with  $d$  being the projected distance in arcsec. Note that the fits could be affected by the missing flux around the systemic velocity.

This figure "f2.jpg" is available in "jpg" format from:

<http://arxiv.org/ps/astro-ph/0701284v1>